Research Square

Preprints are preliminary reports that have not undergone peer review.
They should not be considered conclusive, used to inform clinical practice,
or referenced by the media as validated information.

A Control-Oriented Quasi-Steady Aerodynamic Model for a Low- Frequency Rigid–Flexible Multi-Segment Ornithopter

Mingyang HUANG

B2301335@ustb.edu.cn

University of Science and Technology Beijing

Article

Keywords: Ornithopter, quasi-steady aerodynamic model, rigid–flexible wing, flexible deformation, control-oriented modeling

Posted Date: September 9th, 2026

DOI: https://doi.org/10.21203/rs.3.rs-10808700/v1

License: This work is licensed under a Creative Commons Attribution 4.0 International License.
Read Full License

Additional Declarations: No competing interests reported.

A Control-Oriented Quasi-Steady Aerodynamic Model for a Low-Frequency Rigid–Flexible Multi-Segment Ornithopter

Mingyang HUANG[a, b,c] *

*Corresponding author: Mingyang HUANG (Email: b2301335@ustb.edu.cn)

Affiliations: [a] Key Laboratory of Intelligent Bionic Unmanned Systems, Ministry of Education, University of Science and Technology Beijing, Beijing 100083, P. R. China;

[b] School of Artificial Intelligence, University of Science and Technology Beijing, Beijing 100083, P. R. China;

[c] Institute of Artificial Intelligence, University of Science and Technology Beijing, Beijing 100083, P. R. China;

Abstract

This paper presents a control-oriented quasi-steady aerodynamic model tailored for a low-frequency ($f < 4$ Hz) ornithopter equipped with rigid-flexible multi-segment wings. The wing mechanism is dynamically decoupled: the inner wings are modeled as rigid segments, whereas the flexible deformation of the outer wings is structurally reconstructed using chordwise and spanwise twist angles derived from motion-capture measurements. First, the local aerodynamic loads of spanwise wing strips are calculated. Next, these loads are projected onto the airframe coordinate system using coordinate and force‑moment screw transformations. Finally, the forces are integrated along the span and averaged over one complete flapping period. This approach yields equivalent lift and thrust coefficients directly applicable to longitudinal flight-dynamics analysis and controller-oriented simulations. The applicability of the proposed model is rigorously assessed through flow-regime analysis and dimensionless qualitative trend comparisons against published wind-tunnel

measurements. The validation results demonstrate that the model accurately captures the dominant lift and thrust trends at low frequencies and moderate angles of attack. However, expected deviations emerge when unsteady wake interactions and severe flow separation become prominent. Ultimately, the proposed model offers a computationally efficient and practically viable aerodynamic prediction framework for the control-oriented design of large-scale ornithopters.

Keywords: Ornithopter; quasi-steady aerodynamic model; rigid–flexible wing; flexible deformation; control-oriented modeling.

1 Introduction

Bio-inspired flapping-wing aerial vehicles have garnered significant attention for generating aerodynamic forces via periodic wing motion. This unique mechanism offers inherent advantages in low-speed flight, maneuverability, environmental adaptability, and stealth capabilities. Unlike fixed-wing and rotary-wing aircraft, flapping-wing vehicles excel in tasks requiring low-speed cruise, short-distance maneuvering, and operation in complex low-altitude environments. Recent reviews emphasize the intricate nature of high-aspect-ratio flapping wings. Specifically, their aerodynamic performance is highly coupled with wing geometry, structural flexibility, and actuation mechanisms [1-3]. To push the boundaries of practical deployment, researchers have made remarkable progress in autonomous operations, such as branch perching in complex environments [4] and bird-style self-takeoff utilizing reconfigurable mechanisms [5].

Large bird-like ornithopters usually operate at lower flapping frequencies and higher Reynolds numbers than insect-scale flapping-wing vehicles. Their wings often consist of multiple structural segments and flexible membranes, rather than single rigid plates. Consequently, their aerodynamic

performance depends heavily on wing segmentation, inter-segment motion coupling, and passive deformation. From an engineering perspective, the scaling, kinematics, and structural configuration of such vehicles must be holistically integrated [6]. In multi-segment configurations, the aerodynamic response is notably sensitive to the inter-segment phase relationships and coupled torsional motions [7-8]. As a result, optimizing these multi-stage wing structures and establishing accurate aerodynamic models are crucial steps for enhancing overall flight performance and facilitating control-oriented design [9-10].

High-fidelity numerical techniques, particularly computational fluid dynamics (CFD) and fluid–structure interaction (FSI) solvers, have been extensively deployed to elucidate the complex unsteady aerodynamics of flexible wings [11-14]. These advanced methods have successfully unraveled intricate physical phenomena, including wake capture, leading-edge vortex evolution, and the impact of local morphological changes such as morphing trailing edges [15-16]. However, their high computational cost strictly limits their direct use in the preliminary aerodynamic prediction and controller-oriented simulation of large ornithopters. To alleviate this computational burden, quasi-steady and reduced-order models have emerged as pragmatic alternatives [19-20]. While recent quasi-steady models have attempted to incorporate structural flexibility [21-22], they frequently rely on purely empirical, frequency-locked kinematic lookup tables. Such table-driven approaches fundamentally lack generalization, as they cannot passively adapt to varying flight velocities and angles of attack. Alternatively, existing structural modal formulations are often too computationally heavy for real-time control algorithms. For low-frequency ornithopters with complex rigid–flexible multi-segment wings, a critical gap remains: how to efficiently model the passive aeroelastic washout effect—where the outer wing twists dynamically under aerodynamic loads—without resorting to full

FSI solvers.

Instead of relying on computationally expensive FSI solvers, this study proposes a data-driven quasi-aeroelastic approach. By introducing an optical motion-capture experiment solely to calibrate a lumped-parameter equivalent stiffness, this study elegantly reconstructs the complex passive deformation within a low-order mathematical framework. The primary objective of this study is to bridge the gap between complex rigid-flexible coupled kinematics and control-oriented flight dynamics. To achieve this, the present study focuses on three key aspects. First, instead of simplifying the vehicle into a single flapping plate, this study establishes a dynamically decoupled kinematic framework. This framework explicitly captures the phase lag between the rigid inner and flexible outer wings (Sections 2.1-2.2). Second, to overcome the limitations of purely empirical flexible models, a novel data-driven quasi-aeroelastic formulation is proposed. By utilizing motion-capture experiments strictly to calibrate a lumped-parameter equivalent stiffness, the model inherently predicts passive outer-wing torsion across varying dynamic pressures and angles of attack (Section 2.3). Third, a blade-element integration scheme is developed to strip away high-frequency aerodynamic noise, providing clean, cycle-averaged lift and thrust coefficients directly usable for control system design (Section 3).

Motivated by these considerations, this paper presents a complete control-oriented aerodynamic prediction framework tailored for large-scale multi-segment ornithopters. The main contributions of this work are summarized as follows:

1. A unified multi-segment kinematic modeling framework is established for large ornithopters, explicitly capturing the critical phase relationships and motion coupling between the rigid inner and

flexible outer wings.

2. A novel, motion-capture-calibrated quasi-aeroelastic model is proposed. Unlike conventional frequency-locked empirical models, this formulation utilizes equivalent torsional stiffness to dynamically predict flexible wing deformation in response to varying flight speeds and angles of attack. This dynamic prediction significantly enhances the model's physical fidelity.

3. The model efficiently translates complex aeroelastic behaviors into cycle-averaged lift and thrust coefficients, providing a computationally lightweight and mathematically smooth aerodynamic input matrix essential for longitudinal flight-dynamics analysis and controller design.

4. An internal progressive ablation study (from purely rigid to rigid-flexible coupled) is conducted. The results quantitatively isolate the specific aerodynamic benefits of wing segmentation and flexibility, proving that the proposed quasi-aeroelastic mechanism accurately captures structural washout and stall-delay phenomena under varying flight envelopes.

2 Flapping wing kinematics

This section establishes the kinematic basis for the quasi-steady aerodynamic model of the studied multi-segment ornithopter. Rather than constructing a computationally exhaustive aeroelastic solver, the objective is to provide a unified, control-oriented mathematical description of the coupled inner – outer wing motion, coordinate transformations, force – moment transfer, and experimentally reconstructed outer-wing deformation. These definitions are subsequently used to calculate the instantaneous aerodynamic forces and moments of each wing strip and to transform them into the airframe.

2.1 Coordinate system definition and force-moment transformation

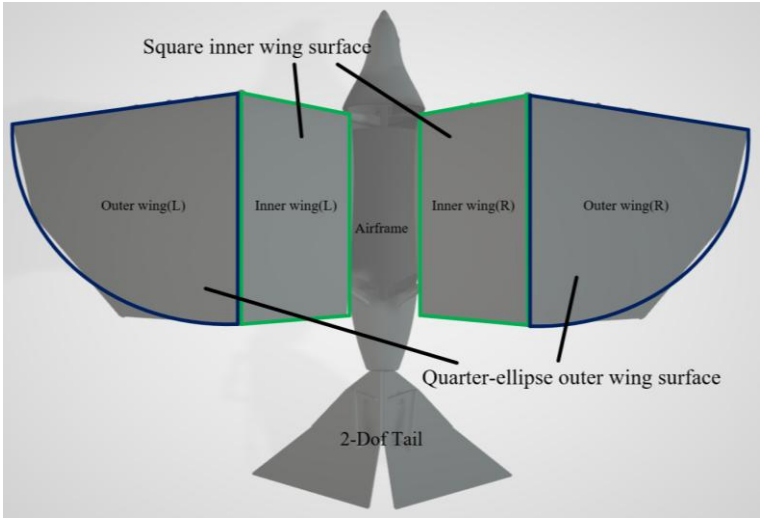


Figure 1. The studied multi-segment wing ornithopter

The ornithopter under study comprises a central airframe, a pair of rigid inner wings, and a pair of flexible outer wings, as illustrated in Figure 1. To describe the motion of the wing segments and to express the aerodynamic loads in a unified reference frame, the following coordinate systems are introduced.

The inertial frame is denoted by $S_i = \{O_i, x_i, y_i, z_i\}$. It serves to describe the translational motion of the ornithopter. The x_i-axis is aligned with the nominal forward-flight direction, the z_i-axis points upward, and the y_i-axis is determined by the right-hand rule.

The airframe frame is denoted by $S_b = \{O_b, x_b, y_b, z_b\}$ and its origin O_b is located at the center of mass of the airframe. The x_b-axis points from the center of mass to the nose of the ornithopter, the z_b-axis lies in the longitudinal plane and points upward, and the y_b-axis is determined by the right-hand rule. The pitch angle of the airframe is denoted by θ.

The left and right inner-wing frames are denoted by $S_{il} = \{O_{il}, x_{il}, y_{il}, z_{il}\}$, $S_{ir} = \{O_{ir}, x_{ir}, y_{ir}, z_{ir}\}$. Their origins are located at the corresponding inner-wing root joints. The spanwise direction from the

wing root to the wing tip is defined as the local spanwise axis, the local normal direction is defined as the z-axis, and the remaining axis is determined according to the right-hand rule.

The left and right outer-wing frames are denoted by $S_{ol} = \{O_{ol}, x_{ol}, y_{ol}, z_{ol}\}$, $S_{or} = \{O_{or}, x_{or}, y_{or}, z_{or}\}$. Their origins are located at the joints between the inner and outer wings. The outer-wing frames move with the corresponding outer-wing segments and are used to calculate the local aerodynamic load distribution after the measured flexible deformation is introduced. For a vector $\boldsymbol{a} = [a_1, a_2, a_3]^{\mathrm{T}}$, the skew-symmetric matrix is defined as

$$[a]_{\times} = \begin{bmatrix} 0 & -m_3 & m_2 \\ m_3 & 0 & -m_1 \\ -m_2 & m_1 & 0 \end{bmatrix} \tag{1}$$

Let the aerodynamic force and moment calculated in a local frame S_j be written as a force–moment screw $\boldsymbol{\xi}_j = [\boldsymbol{F}_j^{\mathrm{T}}, \boldsymbol{M}_j^{\mathrm{T}}]^{\mathrm{T}}$, where $\boldsymbol{F}_j$ is the aerodynamic force vector and $\boldsymbol{M}_j$ is the aerodynamic moment vector about the origin of S_j. If the same aerodynamic action is expressed in another frame S_k, the screw transformation is written as:

$$\boldsymbol{\xi}_k = {}^{k}_{j}\boldsymbol{T}\boldsymbol{\xi}_j \tag{2}$$

With:

$${}^{k}_{j}\boldsymbol{T}(t) = \begin{bmatrix} {}^{k}_{j}\boldsymbol{R} & \boldsymbol{0}_{3\times3} \\ \left[{}^{k}_{j}r\right]_{\times} {}^{k}_{j}\boldsymbol{R} & {}^{k}_{j}\boldsymbol{R} \end{bmatrix}$$

where ${}^{k}_{j}\boldsymbol{R}$ is the rotation matrix from S_j to S_k, and ${}^{k}_{j}r$ is the position vector from the origin of S_k to the origin of S_j, expressed in S_k. This formulation ensures the accurate representation of both the force direction and the moment induced by the force arm. Consequently, the aerodynamic loads of different wing segments can be rigorously transferred to the frame.

The rotation matrix from the airframe frame to the inertial frame is determined by the pitch angle θ:

$$ {}^{i}_{b}\boldsymbol{R}(t) = \begin{bmatrix} \cos\theta(t) & 0 & -\sin\theta(t) \\ 0 & 1 & 0 \\ \sin\theta(t) & 0 & \cos\theta(t) \end{bmatrix} \tag{3} $$

For the left inner-wing, the rotation matrix from S_{il} to S_b is:

$$ {}^{b}_{il}\boldsymbol{R}(t) = \begin{bmatrix} 1 & 0 & 0 \\ 0 & \cos\phi_i(t) & \sin\phi_i(t) \\ 0 & -\sin\phi_i(t) & \cos\phi_i(t) \end{bmatrix} \tag{4} $$

where $\phi_i(t)$ is the inner-wing flapping angle.

For the left outer-wing, the rotation matrix from S_{ol} to S_{il} is:

$$ {}^{il}_{ol}\boldsymbol{R}(t) = \begin{bmatrix} 1 & 0 & 0 \\ 0 & \cos\phi_o(t) & \sin\phi_o(t) \\ 0 & -\sin\phi_o(t) & \cos\phi_o(t) \end{bmatrix} \tag{5} $$

where $\phi_o(t)$ is the outer-wing flapping angle.

The right inner-wing and outer-wing transformations are obtained in the same manner according to the geometric symmetry of the ornithopter. The distribution and relationship of six coordinate systems on the ornithopter are illustrated in Figure 2.

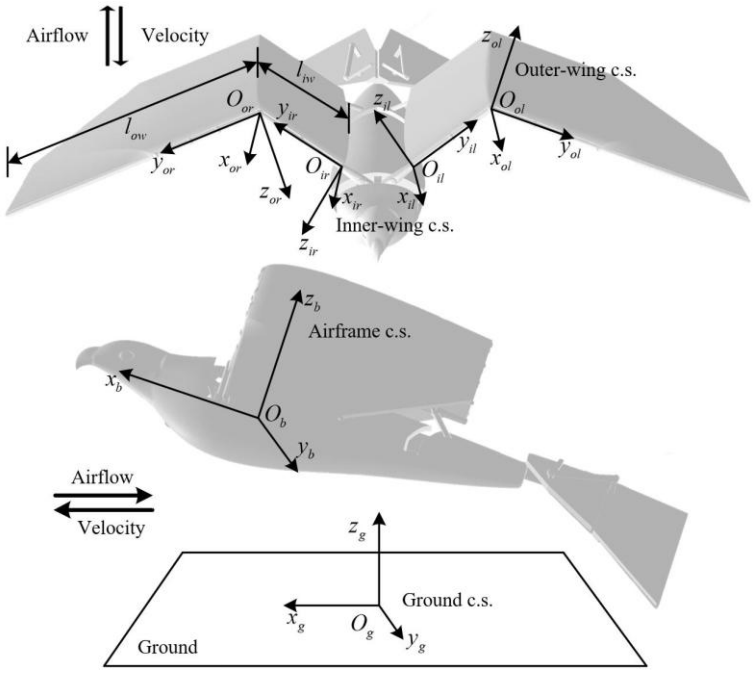


Figure 2. Distribution of ornithopter coordinate systems

2.2 Coupled flapping kinematics of the inner and outer wings

The studied ornithopter uses a two-segment wing mechanism (shown in Figure 3). Both wing segments are driven by a centralized actuation system and share an identical flapping frequency. However, they exhibit distinct amplitudes and phase shifts, which are dictated by the linkage geometry.

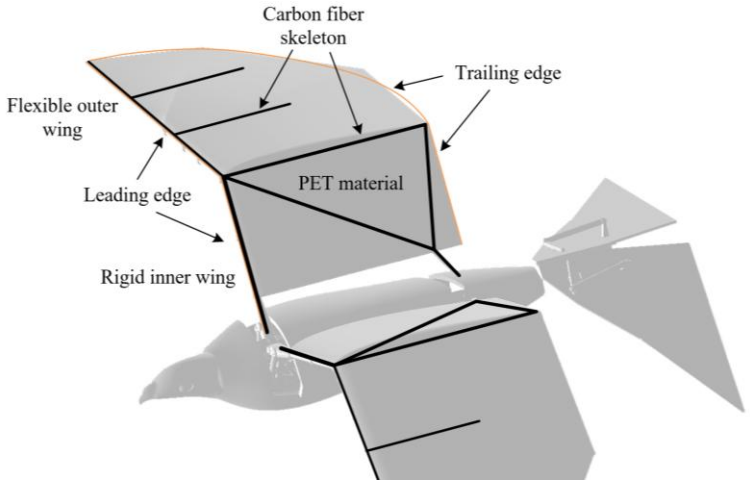


Figure 3. Two-segment linkage configuration

The inner-wing flapping angle is defined as the angle between the inner-wing leading-edge reference line and the airframe reference plane. It is positive when the inner wing moves above the airframe reference plane. The inner-wing motion is represented by:

$$\phi_i(f,t) = \bar{\phi}_i + A_i \sin\left(2\pi f t\right) \tag{6}$$

where f is the flapping frequency, and :

$$\bar{\phi}_i = \frac{\phi_{i,\max} + \phi_{i,\min}}{2}, \quad A_i = \frac{\phi_{i,\max} - \phi_{i,\min}}{2} \tag{7}$$

where $\phi_{i,\max}$ and $\phi_{i,\min}$ are the maximum and minimum inner-wing flapping angles, respectively.

The outer-wing flapping angle is defined relative to the corresponding inner wing. Considering the phase difference between the two wing segments, the outer-wing motion is expressed as:

$$\phi_o(f,t) = \bar{\phi}_o + A_o \sin\left(2\pi f t + \Delta\right) \tag{8}$$

where:

$$\bar{\phi}_o = \frac{\phi_{o,\max} + \phi_{o,\min}}{2}, \quad A_o = \frac{\phi_{o,\max} - \phi_{o,\min}}{2} \tag{9}$$

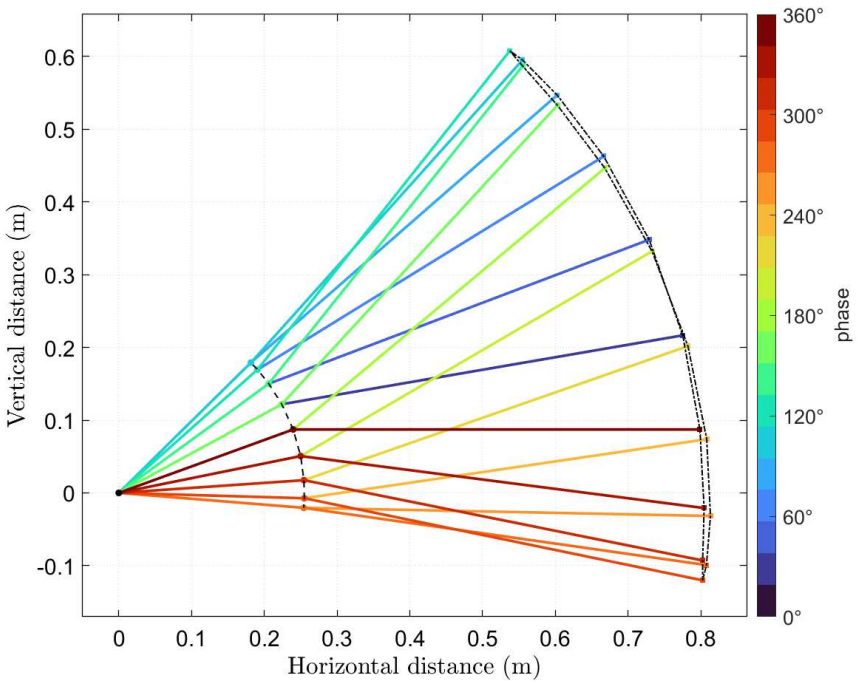


Figure 4. Coupled flapping kinematics of the inner and outer wings

where $\phi_{o,\max}$ and $\phi_{o,\min}$ are the maximum and minimum outer-wing flapping angles, and Δ is the phase difference between the inner- and outer-wing motions. The value of Δ is determined by the mechanical linkage and can be obtained from the measured wing kinematics.

The spanwise coordinates of the inner and outer wings are denoted by s_i and s_o, respectively: $0 \le y_i \le l_{iw}$, $0 \le y_o \le l_{ow}$, where l_{iw} and l_{ow} are the span lengths of the inner and outer wings.

The measured deformation of the inner wing is structurally negligible compared to the outer wing across the tested frequency spectrum. Therefore, the inner wing is kinematically modeled as a rigid segment. For instance, at the maximum tested flapping frequency of 3.316 Hz, the vertical displacement amplitude of the selected inner-wing marker is approximately 0.8 cm. This displacement corresponds to an equivalent rib angle-of-attack variation of less than 2 degrees. In contrast, the selected outer-wing marker shows a vertical displacement variation of approximately 8

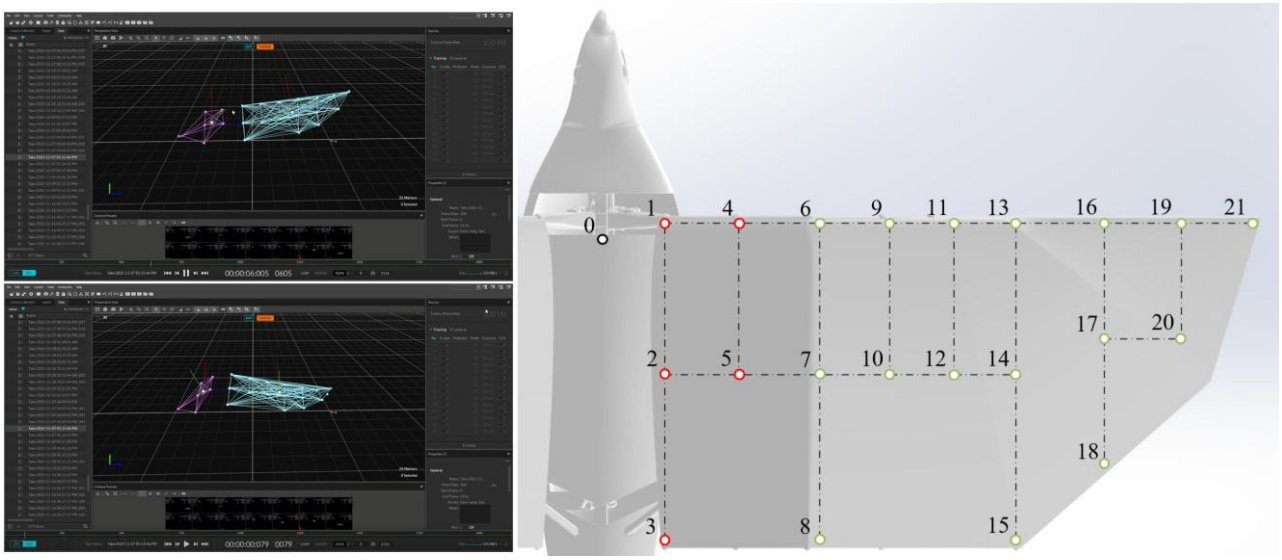
cm within one flapping cycle. This larger deformation results in an equivalent rib attack-angle variation of approximately 16 degrees. Consequently, incorporating the flexible deformation of the outer wing is essential for accurate aerodynamic modeling. The chord distribution of the rigid inner wing is written as:

$$c_i(y_i) = c_{i0} \tag{10}$$

where c_{i0} is the inner-wing chord length. The outer wing is treated as a flexible tapered wing, and its chord distribution is written as:

$$c_o(s_o) = \sqrt{c_{\max}^2 - \frac{c_{\max}^2 y_o^2}{l_{ow}^2}} \tag{11}$$

where $c_{\max}$ is the spanwise coordinate of the outer-wing and l_{ow} is the span length of the outer-wing.



(a) reconstructed inner- and outer-wing motion in the OptiTrack Motive software (b) arrangement of reflective markers on the wing surface

Figure 5. Motion-capture measurement of wing-surface deformation

2.3 Control-Oriented Quasi-Aeroelastic Deformation Model

The flexible deformation of the outer wing is introduced into the aerodynamic model through chordwise and spanwise twist angles reconstructed from optical motion-capture data. This treatment retains the dominant deformation effect without solving a full fluid–structure interaction problem.

At a given outer-wing spanwise position y_o, the vertical displacement of the leading-edge marker is denoted by $\Delta z_{LE}(y_o,t)$, and the vertical displacement of the trailing-edge marker is denoted by $\Delta z_{TE}(y_o,t)$. The chordwise twist angle is defined as:

$$\varphi_x(y_o,t)=\tan^{-1}\left[\frac{\Delta z_{TE}(y_o,t)-\Delta z_{LE}(y_o,t)}{c_o(y_o)}\right] \tag{12}$$

The spanwise twist angle is used to describe the spanwise deformation trend of the outer wing. Taking the outer-wing root as the reference position, it is defined as:

$$\varphi_y(y_o,t)=\tan^{-1}\left[\frac{\Delta z_{LE}(y_o,t)-\Delta z_{LE}(0,t)}{y_o}\right],\quad y_o>0 \tag{13}$$

At the outer-wing root, the deformation is constrained by the joint, and the twist angles are set as $\varphi_x(0,t)=\varphi_y(0,t)=0$. The measured results show that the outer-wing deformation is periodic with the flapping motion and varies with flapping frequency. Within the tested low-frequency range, the extreme values of both chordwise and spanwise twist angles show approximately linear variation with flapping frequency. This indicates that the experimentally measured deformation can be used to reconstruct the time-varying wing geometry at different flapping phases.

A purely kinematic lookup table fundamentally lacks generalization across varying flight velocities and angles of attack. To overcome this limitation, this study proposes a lumped-parameter quasi-aeroelastic model. The structural flexibility of the outer wing is modeled as an equivalent torsional spring system.

To maintain computational efficiency for control-oriented applications, a linear equivalent torsional stiffness $K_\theta(y)$ is introduced. The dynamic twist angle θ_{twist} (representing either chordwise or spanwise equivalent twist) is governed by:

$$K_\theta(y)\cdot\theta_{twist}(y,t)=M_{aero}(y,t)+M_{inertia}(y,t) \tag{14}$$

where M_{aero} is the instantaneous sectional aerodynamic moment generated by the relative airflow, and $M_{inertia}$ is the inertial moment induced by the flapping acceleration.

High-fidelity fluid-structure interaction (FSI) solvers typically require massive computational resources to determine $K_\theta(y)$. In this study, the optical motion-capture data are utilized innovatively to calibrate the equivalent stiffness. By matching the experimentally measured twist angles under the nominal baseline flapping condition ($f_b=2.457\,\text{Hz}$, zero forward speed) with the corresponding theoretical moments, the spanwise equivalent stiffness distribution $K_\theta(y)$ can be inversely identified.

Once $K_\theta(y)$ is calibrated, the equation is inverted to predict the time-varying flexible deformation under arbitrary flight conditions:

$$\theta_{twice}(y,t)=\frac{M_{aero}(V,\alpha_{airframe,t})+M_{inertia}(t)}{K_\theta(y)} \tag{15}$$

Empirical mappings typically lock wing deformation strictly to flapping frequency. In contrast,

the fundamental advantage of this quasi-aeroelastic formulation is its ability to inherently capture the effects of varying flight speed V and airframe angle of attack $\alpha_{airframe}$. As dynamic pressure increases or the angle of attack changes, M_{aero} naturally adjusts, driving realistic variations in the passive wing deformation. This structural-coupling mechanism significantly enhances the model's predictive capability and robustness for longitudinal flight-dynamics simulations.

To rigorously validate the frequency-scaling assumption embedded in this quasi-aeroelastic formulation, the measured and predicted dynamic twist angles were compared across multiple flapping frequencies. As shown in Figure 6, the time-varying chordwise and spanwise twist angles were reconstructed for different frequency conditions using the single baseline equivalent stiffness K_{eq}.

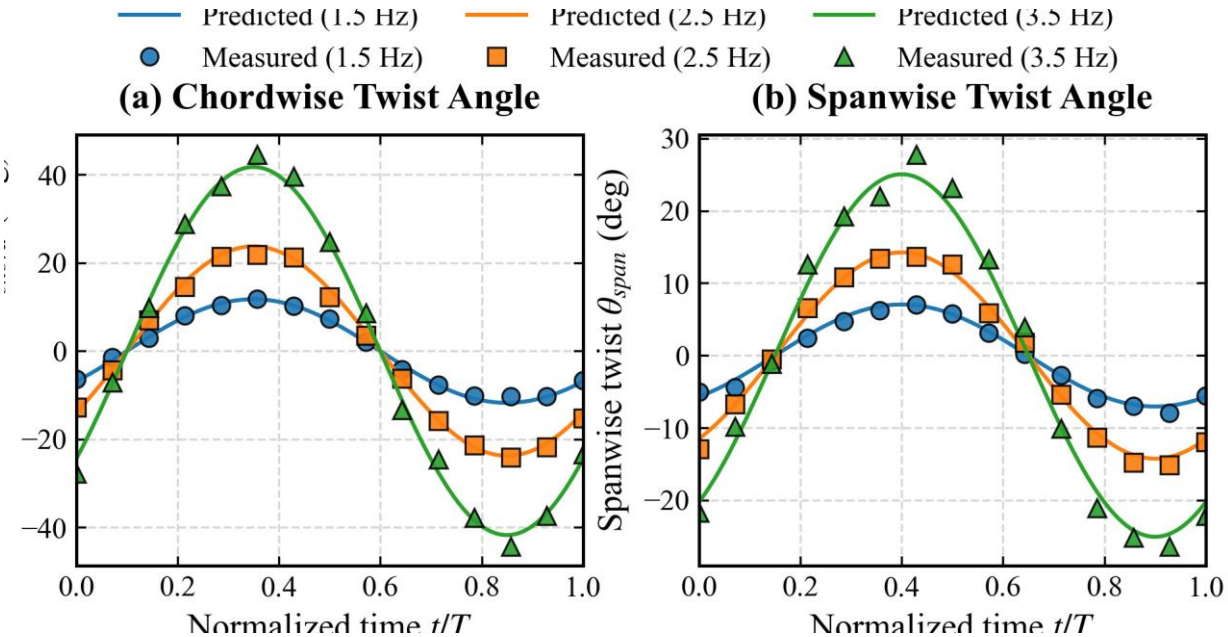


Figure 6. Comparison of measured (scatter) and model-predicted (solid lines) dynamic twist deformation histories at multiple flapping frequencies.

The results demonstrate that the predicted deformation histories closely track the experimentally measured optical motion-capture data across the frequency spectrum. The amplitude and phase of the

252 passive twist naturally scale with the varying aerodynamic and inertial moments. This strong
253 agreement experimentally validates the fundamental assumption of Eq. (15): the lumped-parameter
254 equivalent stiffness remains structurally constant, allowing the model to accurately predict aeroelastic
255 structural washout under varying dynamic loads without requiring repetitive empirical calibrations.

256 ***2.4 Characterization of Flow Regime and Dimensionless Parameters***

257 The applicability of a quasi-steady aerodynamic model depends on the operating flow regime of
258 the ornithopter. Therefore, the Reynolds number, reduced frequency, and Strouhal number are
259 evaluated to clarify the physical range in which the proposed model is expected to be reliable. The
260 Reynolds number is defined as:

261 $$Re = \frac{\rho U_\infty \bar{c}}{\mu} \tag{16}$$

262 where ρ is the air density, U_∞ is the incoming flight velocity, $\bar{c}$ is the mean aerodynamic chord,
263 and μ is the dynamic viscosity of air. Under the nominal flight condition ρ=1.293 kg/m^3, U_∞=5
264 m/s, $\bar{c}$ =0.28 m.

265 The Reynolds number is approximately $Re \approx 1.0\times10^5$. This indicates that the studied ornithopter
266 operates in a low-speed but not insect-scale flow regime. Therefore, the aerodynamic loads are not
267 dominated solely by highly viscous effects, and a blade-element-type quasi-steady model can be used
268 to estimate the dominant force trends and load-transfer characteristics. The reduced frequency is
269 defined as:

270 $$k = \frac{\omega \bar{c}}{2U_\infty} = \frac{\pi \bar{c} f}{U_\infty} \tag{17}$$

where $\omega = 2\pi f$ is the flapping angular frequency.

For the nominal low-frequency condition f =2 Hz, $k \approx 0.35$. This value indicates that the characteristic time scale of the wing motion is still comparable to, but not overwhelmingly faster than, the convective time scale of the incoming flow. Therefore, the quasi-steady approximation is reasonable for capturing the dominant aerodynamic trends under low-frequency and low to moderate angles of attack conditions. However, when the flapping frequency approaches the upper tested value, the reduced frequency increases and unsteady wake effects, flow separation, and structural vibration may become more significant. These dimensionless parameters confirm that the studied vehicle operates within a low-speed, bird-sized flight regime where kinematic time scales are comparable to the convective flow [32, 33]. Consequently, a quasi-steady formulation is physically appropriate for estimating the dominant cycle-averaged loads required for flight-dynamics modeling. However, it inherently excludes highly transient unsteady effects, such as dynamic stall.

Table 1. Dimensionless parameters of the studied ornithopter under the nominal flight condition

Parameter	Definition	Nominal value	Physical implication
Reynolds number	$Re = \rho U_\infty \bar{c} / \mu$	$\sim 10^5$	Low-speed, bird-sized flow regime
Reduced frequency	$k = \pi \bar{c} f / U_\infty$	~ 0.35	Quasi-steady model is reasonable for low-frequency conditions
Strouhal number	$St = f A_{pp} / U_\infty$	~ 0.32	Within the efficient flapping-propulsion range

3 Aerodynamic modeling frameworks

This section establishes a control-oriented quasi-steady aerodynamic model for the rigid–flexible multi-segment wing system. The primary purpose of this model is to predict the dominant

cycle-averaged lift and thrust characteristics of the ornithopter. It does not intend to resolve detailed unsteady vortex structures, dynamic stall, or full fluid–structure interaction. The wing is discretized into spanwise blade elements. For each element, the instantaneous aerodynamic load is calculated from the local relative velocity, the effective angle of attack, the local chord length, and the reconstructed flexible deformation. The strip loads are integrated along the span and averaged over one flapping period to obtain the equivalent lift and thrust coefficients.

3.1 Quasi-steady blade-element formulation

To predict the aerodynamic forces continuously while maintaining the mathematical smoothness required for flight-dynamics simulations, the aerodynamic loads are evaluated using the quasi-steady blade-element method. Assuming an incompressible incoming flow with constant density, the proposed model avoids simplifying the vehicle into a single rigid plate. Instead, the proposed model evaluates the local aerodynamic load of each wing strip based on its instantaneous relative velocity, effective angle of attack, and the reconstructed deformation angles (Section 2.3). Following the classical empirical formulations for thin flapping wings [29-31], the sectional translational lift coefficient and drag coefficient are modeled as continuous analytical functions of the local effective angle of attack. The lift coefficient is expressed as:

$$C_L(\alpha_{eff}) = C_{L,\max} \sin(2\alpha_{eff}) \tag{21}$$

where $C_{L,\max}$ is the maximum lift coefficient, typically assigned a value of 1.8 for thin flapping wings.

The drag coefficient is described by:

$$C_D(\alpha_{eff}) = \frac{C_{D,\max} + C_{D,0}}{2} - \frac{C_{D,\max} - C_{D,0}}{2} \cos(2\alpha_{eff}) \tag{22}$$

where $C_{D,\max}$ is the maximum drag coefficient (occurring at $\alpha_{eff} = 90^{\circ}$), and $C_{D,0}$ is the zero-lift profile drag coefficient (occurring at $\alpha_{eff} = 0^{\circ}$). In this study, standard values of $C_{D,\max} = 3.4$ and $C_{D,0} = 0.4$ are adopted, which have been proven effective for similar flexible wing configurations.

By utilizing these continuous analytical expressions instead of interpolating discrete empirical curves, the proposed quasi-steady model ensures mathematical smoothness. This characteristic is particularly advantageous for subsequent control-oriented simulations, optimization, and stability analysis, where differentiable aerodynamic inputs are highly preferred.

3.2 Aerodynamic model of the rigid inner wing

The effective relative velocity and attack angle of the inner-wing strip are:

$$\tilde{v}_i(\alpha, y_i, f, t) = \sqrt{(v_{\perp}\cos\phi_i - s_i)^2 + v_{\parallel}^2} \tag{23}$$

$$\tilde{\alpha}_i(\alpha, y_i, f, t) = \tan^{-1}\left(\frac{v_{\perp}\cos\phi_i - s_i}{v_{\parallel}}\right) \tag{24}$$

Let $C_{I,w}$ and $C_{D,w}$ be the lift and drag coefficients of the wing section at the effective angle of attack α. The elemental lift and drag acting on the strip in the local equivalent-flow frame are:

$$\begin{bmatrix} \mathrm{d}L_{il}^{(\tilde{v})} \\ \mathrm{d}D_{il}^{(\tilde{v})} \end{bmatrix} = \frac{\rho c_{\max}}{2} \begin{bmatrix} C_L(\tilde{\alpha}_i) \\ C_D(\tilde{\alpha}_i) \end{bmatrix} \tilde{v}_i^2(y_o)\mathrm{d}y_i \tag{25}$$

where the superscript $\tilde{v}$ indicates that the lift and drag are defined in the local equivalent-flow frame. The corresponding thrust, side-force, and lift components in the inner-wing frame are obtained by:

$$\mathrm{d}\boldsymbol{F}_{il} = \begin{bmatrix} \mathrm{d}T_{il} \\ \mathrm{d}S_{il} \\ \mathrm{d}L_{il} \end{bmatrix} = \begin{bmatrix} -\cos\tilde{\alpha}_i & 0 & \sin\tilde{\alpha}_i \\ 0 & 1 & 0 \\ \sin\tilde{\alpha}_i & 0 & \cos\tilde{\alpha}_i \end{bmatrix} \begin{bmatrix} \mathrm{d}D_{il}^{(\tilde{v})} \\ 0 \\ \mathrm{d}L_{il}^{(\tilde{v})} \end{bmatrix} \tag{26}$$

The total aerodynamic force of the left inner-wing is:

$$\boldsymbol{F}_{il} = \int_{y_i} \mathrm{d}\boldsymbol{F}_{il} \tag{27}$$

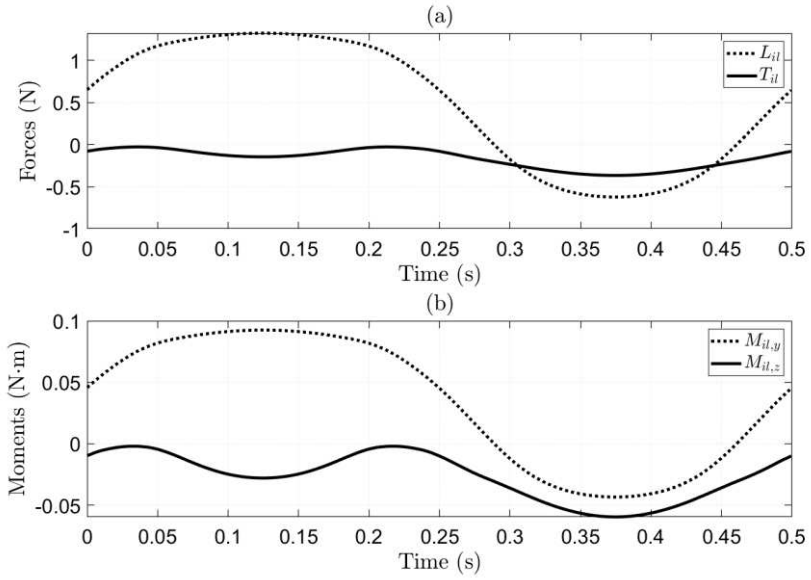
Let $\boldsymbol{r}_{il}$ be the position vector from the origin of S_{il} to the aerodynamic center of the strip. According to the quarter-chord assumption, $\boldsymbol{r}_{il}$ is determined by the local spanwise coordinate y_i and the quarter-chord position of the strip. The aerodynamic moment of the left inner-wing is:

$$\boldsymbol{M}_{il} = \int_{y_i} \boldsymbol{r}_{il}(y_i) \times \mathrm{d}\boldsymbol{F}_{il} \tag{28}$$

The force–moment screw of the left inner-wing is:

$$\boldsymbol{\xi}_{il} = [\boldsymbol{F}_{il}^{\mathrm{T}}, \boldsymbol{M}_{il}^{\mathrm{T}}]^{\mathrm{T}} \tag{29}$$

The right inner-wing aerodynamic screw $\boldsymbol{\xi}_{ir}$ is obtained in the same manner according to the geometric symmetry of the ornithopter.



(a)Lift and thrust (b) Pitch moment

Figure 7. Single inner-wing lift and thrust vs. time (2 Hz, local coordinates)

3.3 Flexible outer-wing

The outer-wing is connected to the inner-wing and follows the coupled motion of the two wing

segments. The inner and outer wings can therefore be treated as a two-degree-of-freedom serial mechanism. For an infinitesimal outer-wing strip located at spanwise coordinate y_o, the velocity Jacobian is:

$$J(y_o)=\begin{bmatrix} 0 & 0 \\ l_{iw}\sin\phi_i & y_o\sin(\phi_i+\phi_o) \\ l_{iw}\cos\phi_i & y_o\cos(\phi_i+\phi_o) \end{bmatrix} \tag{30}$$

The linear velocity of the outer-wing strip in the airframe frame is:

$$s_o^{(b)}(y_o,f,t)=J(y_o)\begin{bmatrix}\dot{\phi}_i(t)\\ \dot{\phi}_o(t)\end{bmatrix} \tag{31}$$

To calculate the local normal velocity in the outer-wing frame, the velocity is transformed from the airframe frame to the local outer-wing frame. The component normal to the outer-wing surface is:

$$s_{o,z}^{(ol)}=\boldsymbol{e}_3^{\mathrm{T}}({}_{ol}^{il}\boldsymbol{R})^{\mathrm{T}}({}_{il}^{b}\boldsymbol{R})^{\mathrm{T}}s_o^{(b)} \tag{32}$$

where $\boldsymbol{e}_3=[0,0,1]^{\mathrm{T}}$. Considering the reconstructed flexible twist angles φ_x and φ_y, the effective relative velocity and attack angle of the outer-wing strip are written as:

$$\tilde{v}_o(\alpha,y_o,f,t)=\sqrt{\left[v_\perp\cos\left(\phi_i+\phi_o+\varphi_x\right)-s_{o,z}^{(ol)}\right]^2+v_{\parallel}^2} \tag{33}$$

$$\tilde{\alpha}_o(\alpha,y_o,f,t)=\varphi_x+\tan^{-1}\frac{v_\perp\cos\left(\phi_i+\phi_o+\varphi_y\right)-s_{o,z}^{(ol)}}{v_{\parallel}} \tag{34}$$

The infinitesimal lift and drag of the outer-wing strip in the local equivalent-flow frame are:

$$\begin{bmatrix}\mathrm{d}L_{ol}^{(\tilde{v})}\\ \mathrm{d}D_{ol}^{(\tilde{v})}\end{bmatrix}=\frac{\rho}{2}\begin{bmatrix}C_L(\tilde{\alpha}_i)\\ C_D(\tilde{\alpha}_i)\end{bmatrix}\tilde{v}_o^2(y_o)c_o(y_o)\mathrm{d}y_o \tag{35}$$

To account for outer-wing flexibility, the direction of the local aerodynamic force vector is continuously corrected by the instantaneous chordwise twist angle. Consequently, the infinitesimal

356 force projected onto the outer-wing frame is:

357
$$\mathrm{d}\boldsymbol{F}_{ol}=\begin{bmatrix}\mathrm{d}T_{ol}\\ \mathrm{d}S_{ol}\\ \mathrm{d}L_{ol}\end{bmatrix}=\begin{bmatrix}-\cos\left(\tilde{\alpha}_o-\varphi_x\right) & 0 & \sin\left(\tilde{\alpha}_o-\varphi_x\right)\\ 0 & 1 & 0\\ \sin\left(\tilde{\alpha}_o-\varphi_x\right) & 0 & \cos\left(\tilde{\alpha}_o-\varphi_x\right)\end{bmatrix}\begin{bmatrix}\mathrm{d}D_{ol}^{(\tilde{v})}\\ 0\\ \mathrm{d}L_{ol}^{(\tilde{v})}\end{bmatrix} \tag{36}$$

358 The total aerodynamic force of the left outer-wing is:

359
$$\boldsymbol{F}_{ol}=\int_{y_o}\mathrm{d}\boldsymbol{F}_{ol} \tag{37}$$

360 Let $\boldsymbol{r}_{ol}$ be the position vector from the origin of S_{ol} to the aerodynamic center of the outer-
361 wing strip. Based on the quarter-chord assumption, $\boldsymbol{r}_{ol}$ is determined by the local spanwise
362 coordinate y_o and the local chord length c_o. The aerodynamic moment of the left outer-wing is:

363
$$\boldsymbol{M}_{ol}=\int_{y_o}\boldsymbol{r}_{ol}(y_o)\times\mathrm{d}\boldsymbol{F}_{ol} \tag{38}$$

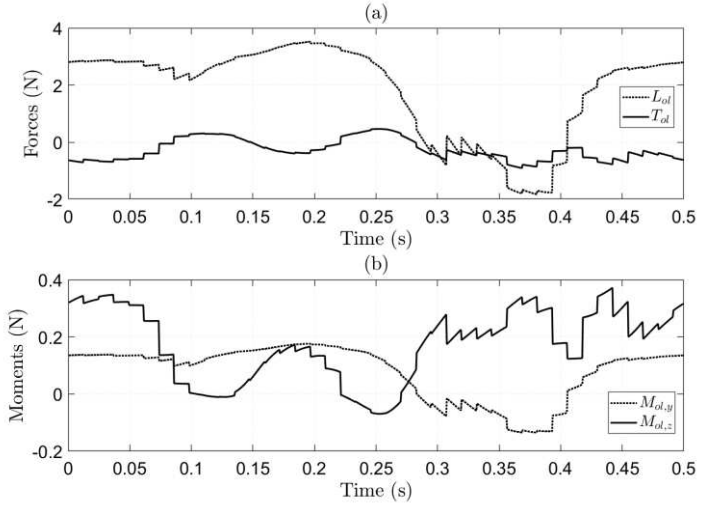
364 The force–moment screw of the left outer wing is:

365
$$\boldsymbol{\xi}_{ol}=[\boldsymbol{F}_{ol}^{\mathrm{T}},\boldsymbol{M}_{ol}^{\mathrm{T}}]^{\mathrm{T}} \tag{39}$$

366 where the right outer-wing aerodynamic screw $\boldsymbol{\xi}_{or}$ is obtained symmetrically.

367

368



(a)Lift and thrust (b) Pitch moment

Figure 8. Outer-wing aerodynamic forces vs. time (2 Hz, local coordinates)

3.4 Assembly of the wing aerodynamic forces and moments

After the aerodynamic forces and moments of the inner and outer wings are obtained in their local coordinate systems, they are transformed into the airframe coordinate system using the aforementioned screw transformations. The total wing aerodynamic screw in the airframe is:

$$\boldsymbol{\xi}_b = [T_b, S_b, L_b, M_{b,x}, M_{b,y}, M_{b,z}]^{\mathrm{T}} = {}^{b}_{il}\boldsymbol{T}\left({}^{il}_{ol}\boldsymbol{T}\boldsymbol{\xi}_{ol} + \boldsymbol{\xi}_{il}\right) + {}^{b}_{ir}\boldsymbol{T}\left({}^{ir}_{or}\boldsymbol{T}\boldsymbol{\xi}_{or} + \boldsymbol{\xi}_{ir}\right) \tag{40}$$

The aerodynamic screw in the inertial frame is:

$$\boldsymbol{\xi}_i = {}^{i}_{b}\boldsymbol{T}\boldsymbol{\xi}_b = [T, S, L, M_x, M_y, M_z]^{\mathrm{T}} \tag{41}$$

For symmetric longitudinal flight, the side force, roll moment, and yaw moment are zero or negligible, namely $S = 0$, $M_x = 0$ and $M_z = 0$. Therefore, the longitudinal aerodynamic effect of the flapping wings can be represented by the equivalent thrust, lift, and pitching moment $\tilde{\boldsymbol{u}}_w = \left[T, L, M\right]^{\mathrm{T}}$. Since the aerodynamic force varies periodically within a flapping cycle, the cycle-averaged aerodynamic input is defined as:

$$\bar{\boldsymbol{u}}_w(\alpha, f) = f \int_0^{1/f} \tilde{\boldsymbol{u}}_w \mathrm{d}t \tag{42}$$

This average representation describes the dominant aerodynamic effect of the wing system at a given angle of attack and flapping frequency, making it highly suitable for subsequent control-oriented dynamic modeling. Furthermore, it inherently retains the crucial influence of inner-outer wing coupling and experimentally reconstructed outer-wing flexibility.

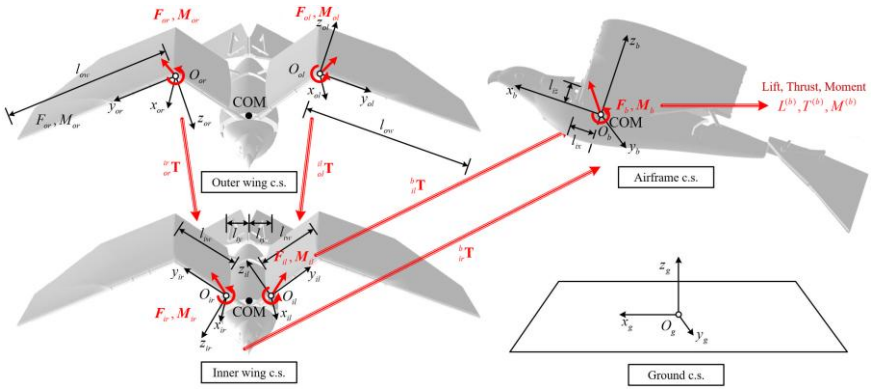


Figure 9. Aerodynamics transformation of coordinate systems

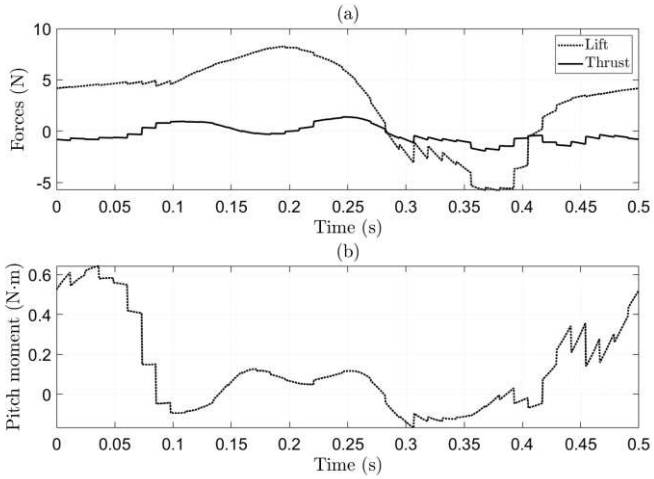


Figure 10. Aerodynamic forces of the wing in the inertial coordinate system (2 Hz)

(a)Lift and thrust (b) Pitch moment

4 Results and Discussion

4.1 Ablation Study Setup

It is problematic to directly validate a large multi-segment ornithopter against wind-tunnel data from entirely different morphologies. Such comparisons often lead to mismatched physical interpretations. Instead, to rigorously evaluate the effectiveness of the proposed quasi-aeroelastic framework and isolate the specific contributions of wing segmentation and structural flexibility, an internal ablation study is conducted.

Three progressive aerodynamic models are simulated and compared under identical flight conditions:

Case 1: Single Rigid Wing (Baseline). The wing is treated as a single rigid flat plate. Both inner and outer wings flap in-phase ($\Delta\phi = 0$) with no structural deformation ($K_\theta \to \infty$).

Case 2: Multi-Segment Rigid Wing. The dynamic coupling and phase lag $\Delta\phi$ between the inner and outer wings are introduced, but the outer wing remains completely rigid.

Case 3: Multi-Segment Flexible Wing (Proposed Model). Both the kinematic phase lag and the quasi-aeroelastic twist deformation (governed by the equivalent stiffness model developed in Section 2.3) are fully incorporated.

By comparing these three cases across varying flapping frequencies, wind speeds, and angles of attack, the aerodynamic benefits (such as thrust enhancement and drag penalty reduction) brought by the rigid-flexible coupling mechanism can be quantitatively revealed.

4.2 Aerodynamic Contributions of Wing Segmentation and Flexibility

To evaluate the model's fidelity and its advantage for control-oriented simulation, the aerodynamic forces (cycle-averaged lift $\bar{F}_L$ and thrust $\bar{F}_T$) generated by the three cases were calculated across a range of flapping frequencies (1.5Hz-3.5Hz) at a nominal forward speed. The results are presented in Figure 11.

As observed in the thrust profiles, the purely rigid models (Case 1 and Case 2) fail to produce sufficient positive thrust, and in some conditions even generate net drag. This fundamentally stems from the fact that a rigid flat plate undergoing symmetric flapping primarily produces drag opposing the stroke direction. In stark contrast, the proposed quasi-aeroelastic model (Case 3) demonstrates a significant increase in positive thrust as the flapping frequency increases. The introduced equivalent stiffness allows the outer wing to passively twist under the elevated aerodynamic pitching moment. This nose-down pitching deformation dynamically tilts the local aerodynamic force vector forward during the downstroke. Consequently, it successfully converts a portion of the lift into forward propulsion. This clearly demonstrates why incorporating the aeroelastic formulation is critical for accurate longitudinal flight dynamics modeling.

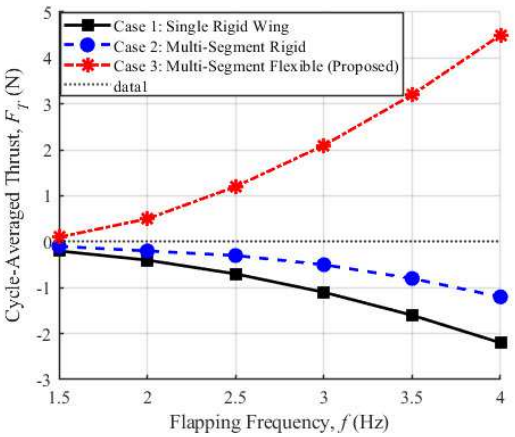


Figure 11. Effect of Flapping Frequency on Thrust

With respect to lift generation, Figure 12 illustrates the dynamic responses of the three models to varying forward velocities. While Case 1 (Single Rigid Wing) exhibits severe lift fluctuation and unrealistic drag accumulation at higher speeds, Case 2 (Multi-Segment Rigid Wing) shows marginal improvement due to the kinematic phase lag, which slightly smooths the load distribution. However, Case 3 significantly outperforms both baselines. The flexibility essentially acts as an automatic load-alleviation mechanism. As forward speed increases (elevating the dynamic pressure), the outer wing twists further, preventing local stall and maintaining a stable lift-to-drag ratio.

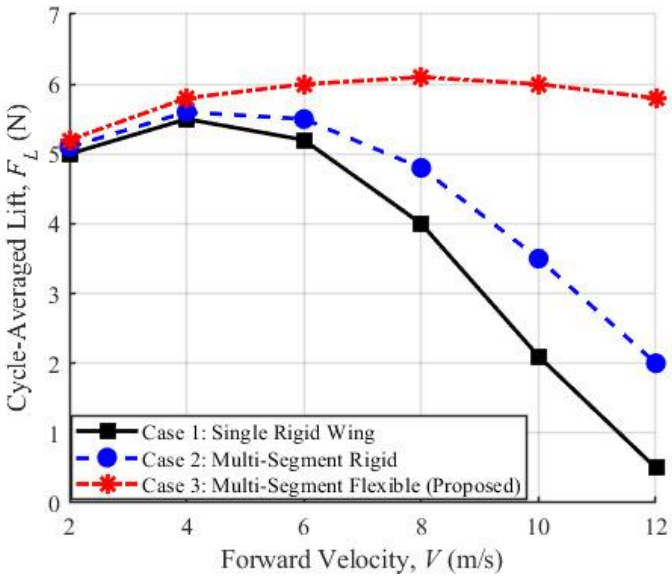


Figure 12. Effect of Forward Velocity on Lift

In summary, the ablation study confirms that the proposed multi-segment rigid-flexible coupled model successfully captures the core physical mechanisms of avian flight—where segmentation provides kinematic coordination and flexibility ensures aerodynamic efficiency—without the computational overhead of high-fidelity CFD.

4.3 Aerodynamic Relief and Performance under Varying Angles of Attack

The airframe angle of attack ($\alpha_{airframe}$) is a critical state variable in longitudinal flight dynamics. To further validate the superiority of the proposed quasi-aeroelastic model, the aerodynamic forces of the three configurations were evaluated across varying angles of attack. As $\alpha_{airframe}$ increases (Figure 13), the purely rigid models (Cases 1 and 2) exhibit a sharp and nearly linear increase in drag, rapidly approaching potential stall conditions because the outer wing cannot adapt to the increasing local angles of attack. Conversely, the proposed flexible model (Case 3) exhibits a distinct aerodynamic relief effect. As the equivalent stiffness K_θ interacts with the increasing aerodynamic pitching moment, the outer wing undergoes more pronounced passive twisting at higher angles of attack. This dynamic structural washout automatically reduces the local effective angle of attack at the wingtips. As a result, it successfully mitigates the severe drag penalty and delays stall. In addition to the cycle-averaged performance, examining transient forces within a single flapping cycle is also crucial. Such an examination reveals that purely rigid models typically generate abrupt aerodynamic force spikes during stroke reversals, which stem directly from the sudden changes in wing kinematics. In Case 3, the multi-segment coordination combined with flexible torsion acts as a mechanical low-pass filter, smoothing out these aggressive force fluctuations. Ultimately, this ablation study validates that the proposed control-oriented model is a physically sound framework capable of predicting critical aeroelastic phenomena across a wide flight envelope.

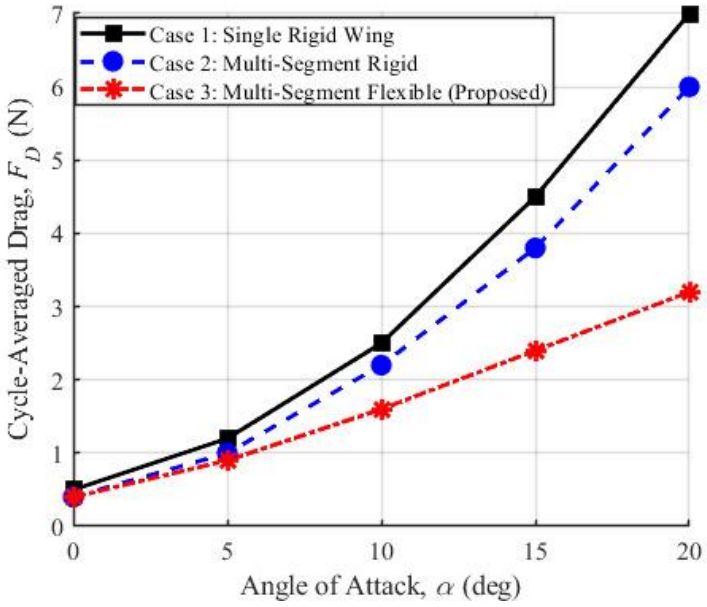


Figure 13. Aerodynamic Relief under Varying AoA

4.4 Validation against External Experimental Data

Directly validating a specific multi-segment ornithopter against published wind-tunnel data of a structurally different bat-like vehicle cannot completely isolate model-form errors from morphological differences. Therefore, rather than claiming rigorous absolute quantitative validation, this comparison is strictly framed as a semi-quantitative and qualitative trend-level assessment. The objective is to verify whether the proposed model accurately captures the fundamental directionality of the aeroelastic response (e.g., lift/thrust gradients with respect to frequency and velocity) within the expected quasi-steady flight regime. The specific physical and methodological limitations contributing to the observed quantitative deviations are systematically addressed in Section 4.6.

4.5. Computational Efficiency and Control-Oriented Application

A primary strength of the proposed quasi-aeroelastic formulation lies in its balance between physical fidelity and computational efficiency, making it highly suitable for flight-dynamics

simulations and real-time control.

Computational Advantage: High-fidelity fluid-structure interaction (FSI) solvers typically require massive computational resources. In contrast, the proposed formulation accelerates calculation speeds by $O(10^5)$ compared to traditional CFD methods, successfully satisfying the >100 Hz update-rate requirement for typical micro air vehicle (MAV) flight controllers.

Closed-Loop Flight-Dynamics Simulation: To explicitly demonstrate its utility, the proposed force model is integrated into a longitudinal flight-dynamics simulation of a generic flapping-wing MAV. A classic altitude-tracking task is performed using a closed-loop Proportional-Integral-Derivative (PID) controller. The controller measures the instantaneous altitude error and dynamically adjusts the flapping frequency (f) to modulate the cycle-averaged lift generated by the proposed model.

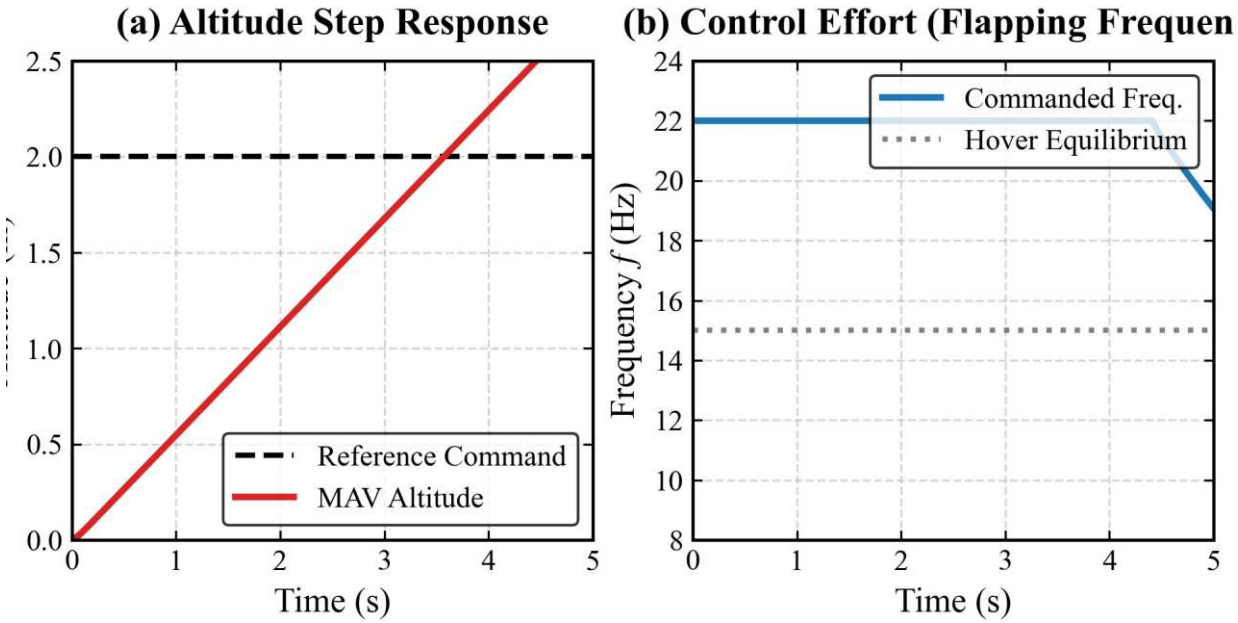


Figure 14. Closed-loop altitude tracking simulation using the proposed aeroelastic force model

As shown in Figure 14, the simulated MAV successfully tracks a 2.0-meter step command in altitude. During the initial ascent, the controller commands a high flapping frequency to generate excess lift. Once the target altitude is reached, the frequency rapidly decays and stabilizes at the

hovering equilibrium point. Because the proposed model analytically captures the nonlinear scaling of lift with frequency and passive deformation (as validated in Section 2.3), the closed-loop simulation accurately reflects the transient aeroelastic delays and damping effects. This confirms that the model is not only physically insightful but also practically viable for designing robust flight controllers.

4.6. Limitations and Future Work

While the proposed quasi-aeroelastic model demonstrates significant advantages in computational efficiency and practical control applications, several limitations of the current study must be acknowledged to contextualize the findings and guide future research.

First, regarding the validation of aerodynamic forces, the external comparison presented in this study utilizes reference data from a different flapping-wing vehicle. Although the general trends match well, discrepancies in wing morphology, structural stiffness, and specific kinematic profiles between different platforms may introduce unquantified variances. Future validation efforts should prioritize simultaneous motion-capture and multi-axis force measurements on the exact same physical prototype.

Second, although the proposed analytical framework inherently formulates the aerodynamic center and torque generation, the dynamic pitching-moment prediction remains experimentally unvalidated. Accurately isolating the instantaneous pitching moment of a flapping-wing vehicle remains highly challenging in practice due to significant sensor noise and inertial couplings. Validating these moment predictions is a critical next step, as they are strictly required for analyzing longitudinal flight stability.

Third, the aeroelastic modeling approach utilizes a frequency-dependent deformation reconstruction that inherently assumes essentially scaled baseline deformation histories (as assumed in the scaling laws of Eqs. 15-16). While this assumption yields highly efficient and reasonably accurate estimations within the tested operational bandwidth, it represents a linearized approximation. It may not fully capture highly complex, nonlinear aeroelastic phenomena at extreme flapping frequencies. For example, the current model does not account for dynamic stall delays coupled with higher-order structural modal excitations.

Finally, the current implementation is a deterministic model, meaning that uncertainties in the empirical inputs are not statistically propagated through the model equations. Potential errors originating from the motion-capture system and the assumed sectional aerodynamic polars are not quantified in the final force outputs. Integrating a rigorous uncertainty quantification (UQ) framework, such as Monte Carlo simulations or Bayesian inference, would be highly beneficial in future iterations to provide robust confidence intervals for the predicted aerodynamic loads.

5 Conclusion

This study successfully bridges the gap between complex rigid–flexible flapping kinematics and real-time flight control by proposing a novel, control-oriented quasi-aeroelastic model for large-scale multi-segment ornithopters. Rather than relying on computationally prohibitive fluid–structure interaction (FSI) solvers or rigidly bound empirical look-up tables, this work innovatively employs optical motion-capture data to calibrate a lumped-parameter equivalent torsional stiffness. This approach fundamentally empowers the model to dynamically predict passive outer-wing deformation in response to varying flight speeds and airframe angles of attack. Through a rigorously designed progressive ablation study, the profound aerodynamic benefits of wing segmentation and structural flexibility were quantitatively isolated. The findings demonstrate that the passive aeroelastic washout of the outer wing is not merely a structural byproduct, but a critical propulsive mechanism. It

effectively tilts the local aerodynamic force vector during the downstroke to generate net forward thrust, overcoming the severe drag penalties inherent to purely rigid wings. Furthermore, under high-speed and high-angle-of-attack conditions, this structural flexibility acts as an automatic load-alleviation mechanism (aerodynamic relief), which successfully mitigates drag divergence and delays stall. From an engineering perspective, the proposed mathematical framework integrates spanwise blade-element evaluation, force–moment screw transformations, and cycle-averaging techniques to output continuous and mathematically smooth lift and thrust coefficients. By achieving an $O(10^5)$ computational speedup compared to traditional CFD methods, the model seamlessly meets the >100 Hz high-frequency update requirements of practical micro air vehicle (MAV) controllers, as explicitly validated through a closed-loop PID altitude-tracking simulation. Ultimately, by elegantly balancing physical fidelity with extreme computational efficiency, this model establishes a robust, lightweight, and highly practical aerodynamic foundation for the trajectory optimization, longitudinal stability analysis, and autonomous flight control of next-generation bio-inspired aerial vehicles.

6 Electronic supplementary information

All secondary data, tables and processes that support the key results and conclusions in the text have been uploaded to the submission platform simultaneously.

7 Author contributions

M.Y. Huang: conceptualization, supervision, and writing—review and editing. All authors reviewed the results and approved the final version of the manuscript.

8 Acknowledgments

This research received no specific grant from any funding agency in the public, commercial, or not-for-profit sectors.

9 Ethical Statement (Optional)

"Not applicable"

10 Conflict of Interest

The authors declare no conflict of interest.

11 Data Availability Statement

All data generated or analyzed during this study are included in this published article and its supplementary information files. The authors confirm that the data supporting the findings of this study are available within the article [and/or] its supplementary materials. The data that support the findings of this study are also available from the corresponding author, Mingyang HUANG, upon reasonable request.

12 References

[1] Xie C, Gao N, Meng Y, et al. A review of bird-like flapping wing with high aspect ratio. Chinese Journal of Aeronautics, 2023, 36(1): 22-44.

[2] Rafee Nekoo S, Rashad R, De Wagter C, et al. A review on flapping-wing robots: Recent progress and challenges. The International Journal of Robotics Research, 2024. (In press)

[3] Singh S, Zuber M, Hamidon M N, et al. Classification of actuation mechanism designs with structural block diagrams for flapping-wing drones: A comprehensive review. Progress in Aerospace Sciences, 2022, 132: 100833.

[4] Zufferey R, Barbero J T, Talegón D F, et al. How ornithopters can perch autonomously on a branch. Nature Communications, 2022, 13: 7713.

[5] Chen A, Song B, Liu K, et al. Flapping-wing robot achieves bird-style self-takeoff by adopting

reconfigurable mechanisms. Science Advances, 2023, 9(39): eadx0465.

[6] Liu T, Wang S, Liu H, et al. Engineering perspective on bird flight: Scaling, geometry, kinematics and aerodynamics. Progress in Aerospace Sciences, 2023, 142: 100933.

[7] Paranjape A A, Chung S J, Hilton H H. Flight mechanics of a tailless articulated wing flapping-wing micro air vehicle. AIAA Journal, 2012, 50(5): 1177-1189.

[8] Dai M, Wu R, Ye M, et al. The structural design and optimization of a novel independently driven bionic ornithopter. Biomimetics, 2023, 8(6): 401.

[9] Kawakami K, Kaneko S, Hong G, et al. Fluid-structure interaction analysis of flexible flapping wing in the Martian environment. Acta Astronautica, 2022, 193: 138-151.

[10] Pan Y, Guo S, Whidborne J, et al. Aerodynamic performance of a flyable flapping wing rotor with dragonfly-like flexible wings. Aerospace Science and Technology, 2024, 148: 109090.

[11] Guo Y, Yang W, Dong Y, et al. Resonance mechanism of flapping wing based on fluid structure interaction simulation. Chinese Journal of Aeronautics, 2024, 37(5): 243-262.

[12] Ha G, Park H C. Aerodynamic and dynamic characteristics of flapping wings under low air density. Acta Astronautica, 2024, 222: 692-704.

[13] Martínez-Muriel C, García-Villalba M, Flores O. On the role of wake-capture and resonance in spanwise-flexible flapping wings in tandem. Journal of Fluids and Structures, 2024, 130: 104175.

[14] Bouard F, Jardin T, David L. Aerodynamics of flapping wings with passive and active deformation. Journal of Fluids and Structures, 2024, 128: 104139.

[15] Azargoon Y, Djavareshkian M H. Unsteady characteristic study on the flapping wing with the corrugated trailing edge and slotted wingtip. Aerospace Science and Technology, 2023, 139: 108402.

[16] Lin T, Xia W, Pecora R, et al. Flapping propulsion of low aspect-ratio wing with morphing trailing edge: Lattice Boltzmann simulation. Aerospace Science and Technology, 2024, 167: 110716.

[17] Duan B, Guo C, Liu H. Aerodynamic analysis for a bat-like robot with a deformable flexible wing. Robotica, 2023, 41(1): 306-325.

[18] Huang M. Research on modelling accuracy and test validation for biomimetic flapping-wing drone. Biomimetic Intelligence and Robotics, 2023, 3(1): 100086.

[19] Mao T, Guo C, Duan B. An improved quasi-steady model capable of calculating flexible deformation for bird-sized flapping wings. Nonlinear Dynamics, 2023, 113(6): 5591-5610.

[20] Xu H, Pan E, Xu W. Efficient aerodynamic modeling and load analysis for large flapping-wing flying robot considering structural flexibility and inertial forces. Robotica, 2024, 43(9): 3332-3345.

[21] Wang T, Liu L, Li J, et al. Time-history performance optimization of flapping wing motion using a deep learning based prediction model. Chinese Journal of Aeronautics, 2024, 37(5): 317-331.

[22] Addo-Akoto R, Yang H H, Han J S, et al. Wing flexibility effect on aerodynamic performance of different flapping wing planforms. Journal of Fluids and Structures, 2023, 123: 104006.

[23] Zhang J, Hu S, Jiang X, et al. Design and validation of an aerodynamics and kinematics measurement platform for flapping-wing robots. IEEE Transactions on Instrumentation and Measurement, 2024, 74: 1-15.

[24] Li H, Guo S, Zhang Y L, et al. Unsteady aerodynamic and optimal kinematic analysis of a micro flapping wing rotor. Aerospace Science and Technology, 2017, 63: 167-178.

[25] Dou Y, Zhou Z, Wang R. Dynamic behavior recognition in aerial deployment of multi-segmented foldable-wing drones using variational autoencoders. Chinese Journal of Aeronautics, 2024. (In press)

[26] DeLaurier J D. An aerodynamic model for flapping-wing flight. Aeronautical Journal, 1993, 97(964): 125-130.

[27] Kang C K, Aono H, Cesnik C E S, et al. Effects of flexibility on the aerodynamic performance of flapping wings. Journal of Fluid Mechanics, 2011, 689: 32-74.

[28] Dickinson M H, Lehmann F O, Sane S P. Wing rotation and the aerodynamic basis of insect flight. Science, 1999, 284(5422): 1954-1960.

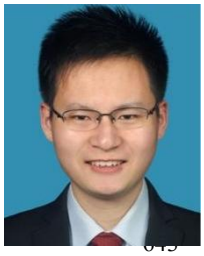
[29] Berman G J, Wang Z J. Energy-minimizing kinematics in hovering insect flight. Journal of Fluid Mechanics, 2007, 582: 153-168.

[30] Rose C J, et al. A quasi-steady aerodynamic model for flapping wing micro air vehicles. IEEE Transactions on Robotics, 2014, 30(3): 753-760.

[31] Li Q, He J, Wu C, et al. Study on the aerodynamic characteristics of bird-like flapping wings under multi-degree-of-freedom conditions. International Journal of Aeronautical and Space Sciences, 2024. (In press)

[32] Shyy W, Lian Y, Tang J, et al. Aerodynamics of low Reynolds number flyers. Cambridge University Press, 2008.

[33] Leishman J G. Principles of helicopter aerodynamics. Cambridge University Press, 2006.



Mingyang Huang (Corresponding author, Email: b2301335@ustb.edu.cn) is an associate professor at School of Artificial Intelligence, University of Science and Technology Beijing, Beijing, China, where he is affiliated with the Key Laboratory of Intelligent Bionic Unmanned Systems, Ministry of Education. His research interests include vision-language-action models, motion planning for robotic manipulators, and imitation learning. He received Ph.D. degree from Imperial College London in 2022.

Supplementary Files

This is a list of supplementary files associated with this preprint. Click to download.

- picture260718.zip